Energy Storage Materials 69 (2024) 103375

Contents lists available at ScienceDirect

Energy Storage Materials

journal homepage: www.elsevier.com/locate/ensm

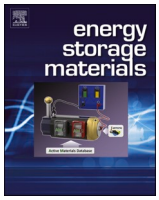

Enhanced performance of lithium metal batteries via cyclic fluorinated ether based electrolytes

Hafiz Ahmad Ishfaq [a,b,c], Carolina Cruz Cardona [d], Elena Tchernychova [a], Patrik Johansson [c,d], Robert Dominko [a,b,c], Sara Drvarič Talian [a,*]

[a] Department of Materials Chemistry, National Institute of Chemistry, Hajdrihova 19, 1000 Ljubljana, Slovenia
[b] Faculty of Chemistry and Chemical Technology, University of Ljubljana, Večna pot 113, 1000 Ljubljana, Slovenia
[c] ALISTORE - European Research Institute, CNRS FR 3104, 15 Rue Baudelocque, Amiens 80039 Cedex, France
[d] Department of Physics, Chalmers University of Technology, 412 96 Gothenburg, Sweden

ARTICLE INFO

Keywords:
Lithium metal batteries
High-voltage cathode
Fluorinated electrolyte
Locally highly concentrated electrolyte
Solvation structure

ABSTRACT

To address the challenges associated with applying high-voltage cathodes in lithium metal batteries (LMBs) there is a need for new electrolytes enabling stable interphases at both electrodes. Here we attack this by using a dioxolane-derived cyclic fluorinated ether, 2,2-bis(trifluoromethyl)-1,3-dioxolane (BTFD), as a fluorinated diluent to a 1,2-dimethoxyethane (DME) based electrolyte. The cells using the resulting BTFD-based electrolytes exhibit higher Coulombic efficiencies for lithium stripping and plating as compared to those using the non-fluorinated ether-based electrolyte. This originates from the reduced formation of 'dead Li' at the anode, as shown by using electrochemical impedance spectroscopy (EIS). In practice, the BTFD-based electrolytes are shown to improve the performance of Li||NMC cells, which is due to the formation of a predominantly inorganic cathode electrolyte interphase (CEI) that suppresses the cathode degradation during cycling. We used X-ray photoelectron spectroscopy (XPS) and scanning transmission electron microscopy (STEM) to characterize the CEIs' overall composition and structure. To obtain more details on the CEI speciation, Raman and nuclear magnetic resonance (NMR) spectroscopies were employed, assisted by molecular level computations. Overall, we demonstrate how the very design of the electrolyte composition influences the performance of LMBs.

1. Introduction

In recent years, there has been a revived global interest in rechargeable lithium metal batteries (LMBs) due to the increasing demand for batteries with high energy densities [1–4]. The lithium metal anode has several advantages, such as a low electrochemical potential (−3.04 V *vs.* SHE) and a high theoretical specific capacity (3860 mAh g^{-1}) [5,6]. There are, however, also several significant challenges; its thermodynamic instability *vs.* the common electrolytes employed in lithium-ion batteries (LIBs) causes the formation of a passivation layer. This, together with inhomogeneous deposition causes low Coulombic efficiency (CE) [7]. Electrolyte engineering is widely recognized as a viable solution [8,9] as it largely determines the nature of the solid electrolyte interphase (SEI) created [10], which ideally should prevent continuous reactions between the anode and the electrolyte and the formation of lithium deposits which are not connected to the lithium reservoir [11,12].

Ether-based electrolytes based on solvents such as 1,2-dimethoxyethane (DME) and 1,3-dioxolane (DOL) are extensively used in LMBs [13]. Their moderate oxidative stabilities (<4 V *vs.* $Li^+/Li°$), however, limit their practical application in LMBs using high-voltage cathodes, such as $LiNi_{0.8}Co_{0.1}Mn_{0.1}O_2$ (NMC811) [14]. Moreover, these electrolytes render unstable cathode electrolyte interphases (CEIs) [15]. Therefore, it is crucial to innovate new electrolytes that enable stable interfaces at both electrodes, *i.e.* SEIs and CEIs, alongside wide electrochemical stability windows (ESWs).

Recently, highly concentrated electrolytes (HCEs) have been employed in LMBs and enabled the use of high-voltage cathode materials [16,17]. In HCEs, the free solvent concentration is decreased, which modifies the lithium-ion (Li^+) solvation and leads to anion-derived SEIs and CEIs [18]. The practical application of HCEs, however, is hampered by their high cost, due to the high content of expensive salts, and poor wettability of electrodes, arising from their high viscosity, which also negatively impacts the ion transport. To address these issues, localized

* Corresponding author.
E-mail address: sara.drvarictalian@ki.si (S. Drvarič Talian).

https://doi.org/10.1016/j.ensm.2024.103375
Received 26 January 2024; Received in revised form 29 March 2024; Accepted 1 April 2024
Available online 1 April 2024

HCEs (LHCEs) were introduced [19,20], which locally retain the Li^+ solvation. These enable advantageous SEIs and CEIs, but have lower viscosities as well as salt contents globally. This is achieved by the addition of poorly Li^+ solvating solvents as diluents [20,21]. Typical examples of diluents are hydrofluoroethers (HFEs), such as 1,2-(1,1,2,2-tetrafluoroethyl) ether (TFEE) [22], 1,1,2,2-tetrafluoroethyl-2,2,3,3-tetrafluoropropylether (TTE) [23], or bis(2,2,2-trifluoroethoxy) methane (BTFM) [24]. All these HFEs are linear molecules, but just as for LIBs [13] combining linear and cyclic solvents has been explored. The Coskun group explored a new class of dioxolane-derived fluorinated cyclic ethers such as 2-(2,2,2-trifluoroethoxy)−4-(trifluoromethyl)−1,3 dioxolane [25], 4-(trifluoromethyl)−1,3-dioxolane [26], and 2,2-dimethoxy-4-(trifluoromethyl)−1,3-dioxolane [27], as solvents in LMB electrolytes. These cyclic fluorinated ether-based electrolytes exhibited significantly enhanced oxidative stabilities, high CEs, and improved cycling performance of LMBs [25,26,28].

Inspired by this, we herein report on the performance and the reaction mechanisms of a cyclic fluorinated ether, 2,2-bis(trifluoromethyl)−1,3-dioxolane (BTFD) (Fig. 1a), as a diluent, *i.e.* with respect to the Li^+ cation a non-solvent, in LMB electrolytes. By strategically incorporating two -CF_3 groups on the O-atom of the dioxolane ring structure, we aimed to enhance the electrochemical stability of the electrolyte while simultaneously maintaining its compatibility with Li metal. This deliberate molecular design of BTFD highlights the importance of rational design principles in advancing LMB electrolytes [29,30]. We compare its performance to that of a linear fluorinated ether, 1,2-bis(2,2,2-trifluoroethoxy) ethane (BTFE) (Fig. 1b), as well as to the linear non-fluorinated ether DME (Fig. 1c). By systematically comparing different molecular designs, we aim to elucidate the influence of structural differences on electrolyte performance, thereby guiding the rational design of fluorinated ethers for LMB electrolytes. Finally we suggest a synergetic electrolyte composition based on the observations made. We determine both physicochemical properties and electrochemical performance *vs.* a Li metal anode as well as in a Li||NMC811 full cell. The electrochemical characterizations are coupled to *post mortem* chemical and structural analyses.

2. Experimental

2.1. Materials

DME (HPLC grade, 99.9%) was purchased from Sigma-Aldrich, BTFE (> 98%) from Fluroyx Labs, and 1,1,2,2-tetrafluoroethyl-2,2,3,3-tetrafluoropropylether (TTE, 99%) and BTFD (99%) from Apollo Scientific. Battery-grade lithium bis(fluorosulfonyl)imide (LiFSI) was acquired from TCI with >98 % purity. NMC811 powder was obtained from MSE supplies, whereas the lithium titanate $Li_4Ti_5O_{12}$ (LTO) powder was purchased from NEI Corporation. Polyvinylidene fluoride (PVdF) from Sigma Aldrich was used as binder in the NMC811 and LTO slurries. Carbon black (SUPER C65) was used as conductive agent in the cathode slurries. The Li metal foil was from FMC (110 μm thick). Cu foil (20 μm thick) was purchased from Goodfellow. Celgard™ 2320 was used as separator in all cells.

2.2. Preparation of electrolytes and electrodes and cell assembly

Solvent drying and electrolyte preparation were done under a protective argon atmosphere in an MBraun glovebox, where O_2 and H_2O contents were followed and kept < 1 ppm. To prepare the electrolytes, the DME solvent was dried using 4 Å molecular sieves for five days, by refluxing it with Na/K alloy overnight, and then purifying it by fractional distillation. The BTFE and BTFD solvents were dried with 4 Å molecular sieves for seven days. The water content in all solvents was determined by Karl Fischer titration (Mettler Toledo, C20) to be < 0.1 ppm. The electrolytes were prepared by weighing stoichiometric amounts of LiFSI into a volumetric flask, dissolving it in a small amount of solvent or solvent mixture, and finally filling the volumetric flask to the marked line. The electrolyte composition was varied with different concentrations of LiFSI (1 M and 2 M) as well as different ratios of fluorinated ether *vs.* DME.

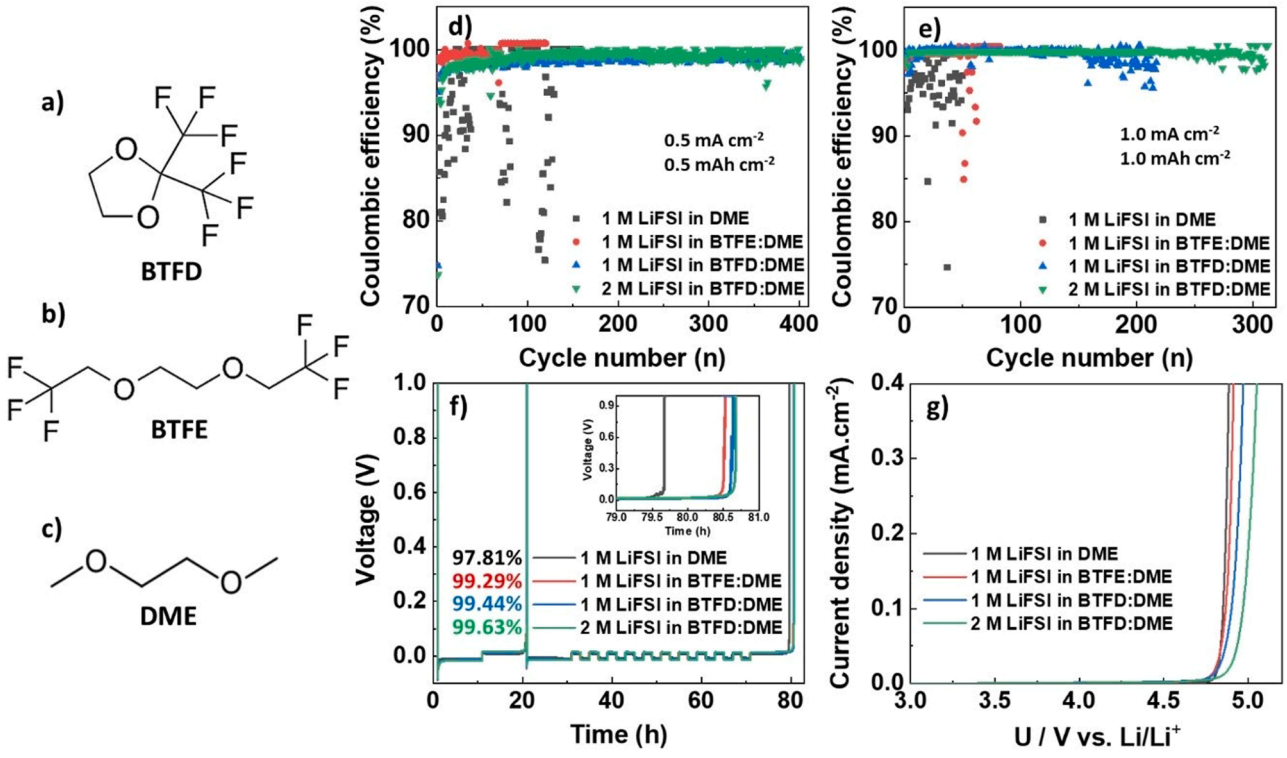

Fig. 1. Chemical structures of (a) BTFD, (b) BTFE, and (c) DME. Coulombic efficiencies of Li stripping and plating of Li||Cu cells using the four different electrolytes from (d,e) galvanostatic cycling and (f) the standard Aurbach method [24], respectively. (g) Oxidative LSV using carbon-coated Al electrodes.

Both LTO and NMC811 cathodes were prepared by conventional slurry-casting using a doctor blade applicator. The LTO cathode slurry was prepared by mixing 80 wt.% active material LTO powder, 10 wt.% C65, and 10 wt.% PVdF binder in NMP using ball milling (30 min, 300 rpm). The resulting slurry was cast onto Cu foil using a doctor blade applicator and dried under vacuum at 80 °C for 2 h. The LTO mass loading varied from 6.4 to 6.6 mg cm^{-2}. The NMC811 slurry was similarly prepared by mixing 90 wt.% NMC811, 5 wt.% PVdF, and 5 wt.% C65 in NMP by ball milling (30 min, 300 ppm), but cast on carbon-coated Al foil and dried under vacuum at 80 °C for 3 h. The NMC811 mass loading varied from 5.4 to 6.2 mg cm^{-2}. Additionally, an NMC811 cathode with a higher mass loading of 16 mg cm^{-2} was also used to evaluate the performance of the BTFD-based electrolytes. LTO and NMC811 cathodes were punched into discs with diameters of 12 mm, pressed by a hydraulic press using a weight of 1.0 t for 30 s, and dried again under vacuum at 90 °C overnight before they were transferred to the glovebox.

All cell preparation was conducted inside an argon-filled MBraun glovebox. For the determination of the CE of lithium stripping and plating, CR2032 coin cells were assembled using a Hohsen Corporation manual crimping tool. For all other cell assemblies, pouch cell casings were employed. In all cell assemblies, the Li metal anodes were 14 mm in diameter and one Celgard 2320 separator was used. The amount of electrolyte added for filling separator pores was 20 μL. In the LTO and NMC811 cells, an additional 10 μL was added to account for the cathode porosity.

2.3. Electrochemical characterization

The efficiency of Li metal stripping and plating was tested using Li||Cu cells with two different current densities: 0.5 mA cm^{-2} with a cutoff areal capacity of 0.5 mAh cm^{-2} and 1.0 mA cm^{-2} with a cutoff areal capacity of 1.0 mAh cm^{-2}. The average Coulombic efficiencies (CEs) were additionally evaluated by applying the standard Aurbach method [31] on the Li||Cu cells with the exact protocol described in [24]. Linear sweep voltammetry (LSV) was employed on Li||carbon-coated Al and Li||Pt cells to explore the oxidative stability of the electrolytes. 30 μL of electrolyte was added to the cells. The cells were tested from the open-circuit voltage (OCV) to 5.1 V *vs.* $Li^+/Li°$ at a scan rate of 0.5 mV s^{-1}. Time-controlled measurements were conducted to assess the critical current density (CCD) [32]. For this purpose, Li||Li cells were subjected to plating and stripping for 1 h, incrementally increasing the current density from 0.2 mA cm^{-2} with steps of 0.2 mA cm^{-2} until reaching the point of short circuit failure, denoted as the CCD.

Electrochemical impedance spectroscopy (EIS) was used to calculate the Li transport numbers (t_{Li}^+) of the electrolytes by the Bruce-Vincent method [33,34]. For these experiments, Li||Li symmetrical cells were allowed to stabilize for 24 h. The EIS spectra were measured in the frequency range of 1 MHz to 100 mHz with a potential amplitude of 10 mV (rms). The polarization potential from which the initial and steady-state currents were determined, was set to 10 mV. Additional EIS spectra were measured in a wider frequency range of 1 MHz to 1 mHz with the 10 mV (rms) potential amplitude, both for pristine and cycled cells. After initial EIS measurements the cells were used for lithium stripping and plating studies using two different conditions: 0.5 mA cm^{-2} with a cutoff areal capacity of 1.0 mAh cm^{-2} for 50 cycles (normal cycling conditions) and 5.0 mA cm^{-2} with a cutoff areal capacity of 10 mAh cm^{-2} for 2 cycles (aggravated cycling conditions). A 10 min rest period was included between the end of the stripping/plating experiment and the EIS measurements on cycled Li||Li cells.

The Li||LTO cells were tested in pouch cells using Cu contacts. These cells were tested in a voltage range of 1.0–2.5 V *vs.* $Li^+/Li°$ at 0.6 C charge and discharge rates. The electrochemical performance of Li||NMC811 cells was evaluated in pouch cells using Al and Cu current collectors. These cells were cycled in two different voltage ranges, *i.e.* 2.7–4.3 V and 2.7–4.6 V *vs.* $Li^+/Li°$ at 0.3 C charge and discharge rates after two formation cycles at 0.1 C. All the electrochemical tests were performed using Biologic VMP3 potentiostat/galvanostat.

2.4. Materials characterization

The densities and viscosities of the electrolytes were measured in the temperature range 0–60 °C at 10 °C intervals using an Anton Paar DMA 4500 M density meter, equipped with a Lovis 2000 M rolling ball viscometer module. The ionic conductivities of the electrolytes were recorded from 0 to 60 °C using an in-house built cell setup using 40 μL of electrolyte and an SP-300 (Biologic) impedance analyzer. All the measurements were performed in an Ar-filled glove box.

The local solvation structures of the electrolytes were studied by both Raman and nuclear magnetic resonance (NMR) spectroscopies. The former used a Ram II Raman spectrometer with a 785 nm excitation laser and *ca.* 2 cm^{-1} resolution, to obtain spectra by averaging over 200 samplings in the range 200–4000 cm^{-1}. The ^7Li and ^{19}F NMR spectra were recorded using an Avance Neo 600 MHz spectrometer (Bruker) and coaxial NMR tubes. The internal standard for the ^7Li NMR spectra was 1 M LiCl in D_2O and for the ^{19}F NMR spectra, it was DMSO-d_6 containing 0.03 wt.% deuterated trifluoroacetic acid (CF_3COOH).

The *post mortem* analysis of the cycled cells was carried out using scanning electron microscopy (SEM), X-ray photoelectron spectroscopy (XPS), and scanning transmission electron microscopy (STEM). For the SEM investigations, the Li electrodes harvested from Li||Li cells were washed with anhydrous DME inside the glove box. For the XPS and STEM analyses, Li||NMC811 cells were cycled for 50 cycles at 0.3 C prior to disassembly inside the glove box to collect both Li and NMC811 electrodes. The electrodes were washed with anhydrous DME and transferred from the glovebox using Ar-filled transfer vessels.

The morphology of the Li deposits was examined with SEM (SUPRA 35VP, Zeiss, Germany). The samples were transferred to the SEM with a vacuum transfer tool to ensure a protective atmosphere. The acceleration voltage was 1.5 kV.

XPS was conducted using a Versaprobe 3 AD (Phi, Chanhassen, US) with a monochromatic Al-$K\alpha_1$ X-ray (1486.7 eV) excitation source. The spectra were acquired on a 200 μm spot size with the charge neutralizer turned on, as the electrodes were placed on a non-conductive double tape, to prevent any possible differential charging of the cycled NMC811 electrodes. High-resolution spectra were measured at 69 eV pass energy and steps of 0.05 eV. Charge neutralization was used, and the energy scale of the XPS spectra was corrected by shifting the C 1 s peak of carbon to a binding energy of 284.8 eV. The XPS spectra were analyzed using the Ulvac-PHI Multipak software. For the fits, the error in the binding energy scale for all the peaks was limited to ±0.2 eV. Shirley background correction was used for all the spectra.

The samples for STEM were prepared inside a FEI Helios Dual Beam system. A randomly selected secondary particle of NMC811 underwent lift-out processes using a focused ion beam and was attached to a Cu TEM grid. Thinning procedures were performed at 30 kV, followed by subsequent steps at 5 and 2 kV to refine the surface and eliminate damaged layers. The samples were then characterized using a JEOL ARM 200CF STEM with spherical aberration correction. The 20.6 mrad convergence angle was set for imaging, and signals within the ranges of 10 – 24 and 95 – 370 mrad were collected for annular bright-field STEM (ABF-STEM) and high-angle annular dark-field STEM (HAADF-STEM), respectively.

2.5. Computational studies

Simulations of impedance spectra were done using a self-written code in Python 3 with standard scientific packages (Matplotlib and NumPy). The code was based on the use of the “mesh method” for solving planar electrical circuits as explained elsewhere [35–37]. For the non-cycled cells, a flat electrode with two distinct SEI layers (compact

and porous) was considered alongside the electrolyte-filled porous separator layer. In the transmission line model (TLM) of the cycled cell, three different porous layers were included - the porous separator, the completely passivated ('dead') high surface area lithium layer, and the high surface area lithium layer where the stripping and plating can still take place ('live' lithium). The last layer indicates that the electrode is/remains porous.

Density functional theory (DFT) calculations were employed primarily to calculate the HOMO and LUMO energy levels and electrostatic potentials (ESPs) of the DME, BTFE, and BTFD solvents, but also to assess the relative strength of the ion-solvent interactions, using a single solvent + Li^+ physical model. Geometry optimized structures of solvents and ion-solvent, verified to be minima by calculating the second derivatives of the energy with respect to nuclear displacements, were obtained by employing the M06–2X functional [38,39] and the 6–311++(d,p) basis set [40,41] within the GAUSSIAN 09 software package [42].

Classical molecular dynamics (MD) simulations were performed to examine the solvation of the lithium ions in relation to the oxygen atoms of the anion, the solvent, and the diluent. The MD simulations were carried out using the LAMMPS [43] software implementing the non-polarizable OPLS-AA force field (FF) [44] and cubic simulation boxes, each containing 100 molecules. Molecular topology files as well as Lennard-Jones and bonded parameters, were all created utilizing the LigParGen server [45–47] and the *fftool* package [48]. To account for electronic screening and enhance the accuracy of the predictions of interionic interactions, a scaling factor of 0.8 was applied to the partial charges of charged ions, owing to the utilization of a non-polarizable FF [49,50]. The simulation procedure initiated with an energy minimization employing conjugate gradients, followed by a three-step equilibration process. First, 1 ns in the microcanonical ensemble (NVE), succeeded by 2 ns in the isothermal-isobaric ensemble (NPT), and then an additional 2 ns in the canonical ensemble (NVT). Subsequently, the production run was carried out in the canonical ensemble (NVT) for 10 ns. All simulations were conducted at a temperature of 300 K and a pressure of 1 atm. A Nosé-Hoover thermostat was employed with a temperature damping of 100 fs and a pressure damping of 1000 fs. Electrostatic interactions were computed using the particle-particle-particle-mesh scheme (PPPM), and periodic boundary conditions were enforced in all directions. Radial distribution functions (RDFs) and coordination numbers (CNs) for subsequent structural analysis were derived from LAMMPS subroutines.

3. Results and discussion

First, we compared the electrochemical characteristics (Fig. 1d-g) of lithium metal anodes using electrolytes based on the cyclic fluorinated ether (BTFD), the linear fluorinated ether (BTFE), and the non-fluorinated ether DME. As described in Note 1 in the Supporting Information, four electrolytes were chosen for further investigation based on different BTFD:DME ratios as well as preliminary performance tests (Figs. S1–S3): 1 M LiFSI in DME (as reference), 1 M LiFSI in BTFE:DME 1:1 (v:v), 1 M LiFSI in BTFD:DME 1:1 (v:v), and 2 M LiFSI in BTFD:DME 1:1 (v:v). We only state the salt concentration and the solvents used from here forth.

The compatibility with the lithium metal anode was tested using galvanostatic cycling of Li||Cu cells at two different current densities and cutoff capacities alongside the method proposed by Aurbach [31] (Fig. 1d-f and Table S1) and shows increased stability of the Li metal anode when using the BTFD-based electrolytes, even at higher current densities.

The CEs and cycling stabilities of the cells increase when adding fluorinated solvents/diluents to the electrolyte, and most improved for the electrolyte compromising the cyclic fluorinated ether (BTFD). The improvement in CEs and cycling stability is accompanied by higher polarisation (Fig. S4, S5, and S6), which could be related to the high viscosity and low ionic conductivity (Fig. S7) of the electrolyte. Finally, we compared the CE and the stability of the BTFD-based electrolytes with a TTE-based electrolyte (1 M LiFSI in TTE:DME) – a commonly used diluent. As illustrated in Fig. S8, the TTE-based electrolyte shows a lower CE (99.19 %, Fig. S8a) and exhibits worse stability (Fig. S8 b and c).

Based on the weaker solvation ability of the fluorinated ethers, one could expect higher oxidation stabilities of the fluorinated solvent-based electrolytes, which indeed is the case for the BTFD-based electrolyte (Fig. 1 g) and also corroborated by the lower HOMO energy for BTFD (Fig. S9). The oxidation stabilities were additionally tested in Li||Pt cells and again the BTFD-based electrolytes showed higher oxidation stabilities than the other electrolytes (Fig. S10). The CCD tests also showed that the BTFD-based electrolytes (4.6 and 5.6 mA cm^{-2}) perform better as compared to both the BTFE-based (3.2 mA cm^{-2}) and the DME-based (2.4 mA cm^{-2}) electrolytes (Fig. S11).

To gain a better understanding of the reasons behind the improved electrochemical performance of the lithium metal anode using the BTFE-based electrolyte we employed EIS. There are only minor differences between the spectra of pristine stabilized cells assembled with different electrolytes, with similar high-frequency arc resistance size (300–420 Ωcm^2) and peak frequency (300 to 350 Hz) (Fig. 2a). The low-frequency contributions are small with the peak frequency between 30 and 100 mHz. The t_{Li}^{+} was determined to increase from 0.35 to 0.65 along: 1 M LiFSI in DME < 1 M LiFSI in BTFE:DME < 1 M LiFSI in BTFD:DME < 2 M LiFSI in BTFD:DME (Fig. S12). The spectra for cycled cells (Fig. S13) assembled with fluorinated electrolytes look analogous with a small high-frequency arc (1–3 Ωcm^2, 20 kHz) and a low-frequency arc of approximately 35 Ωcm^2 and a peak frequency between 10 and 16 mHz (Fig. 2b). The spectrum of the 1 M LiFSI in DME electrolyte cell is markedly different with a large resistive intercept value, 50 Ωcm^2 high-frequency arc (15 kHz) and complex merged low-frequency contributions.

To understand the physical origin of the differences in the spectra, TLM simulations were conducted as reported in [35,51]. We used the TLM models to simulate spectra of non-cycled and cycled cells assembled with 1 M LiFSI in DME and 2 M LiFSI in BTFD:DME as two extreme cases. The TLM circuit for the cycled cells is shown in Fig. 2c, while the meaning of the resistive and capacitive elements and the origin of the "live" porous Li layer and the "dead" Li layer is explained in the Supporting Information (Fig. S14). The circuit for the non-cycled cells is shown in Fig. S15, while the simulated spectra are found in Fig. 2d and Fig. S16. The parameters of the simulated spectra of pristine and cycled electrodes for 2 M LiFSI in BTFD:DME show a decrease in SEI resistance (R_{SEI}) and an increase in SEI capacitance (C_{SEI}) for roughly the same factor (Table S2). The separator contributions (R_{sep1}, R_{sep2}, C_{sep}) remained unchanged, while the diffusional contributions from the 'dead Li' and 'live Li' layers were minimal in comparison with the separator diffusion contributions. We conclude that electrodes cycled with fluorinated ethers have a small high-frequency contribution that stems from large surface area Li deposits on the electrode (which act as a porous electrode) and a low-frequency contribution that is due to diffusion through the separator. This fits well with the electrode morphology observations by SEM (Fig. S17d-f), which show a uniform coverage with an approximate thickness of 5 μm.

For the 1 M LiFSI in DME reference electrolyte we observe a decrease in the contribution of R_{SEI} after cycling, but it is not followed by the same factor increase of the C_{SEI}, which stays roughly the same. The chemical capacitances of the separator (C_{sep}) and 'live Li' layer (C_{live}) also appear to be smaller than expected, with the former decreasing by a factor of 20x (Table S2). This could be explained by a "soft short-circuit" effect [52], which distorts the spectra by decreasing the resistance of the resistive elements and shifting the time constants, increasing peak frequencies. Apart from displaying evidence of short-circuits, the parameters of the spectrum also indicate a thick 'dead Li' layer (large R_{dead} and C_{dead}). In contrast to the cells using fluorinated electrolytes (lower C_{dead}, Supporting Information), the cell with this electrolyte thus suffer both

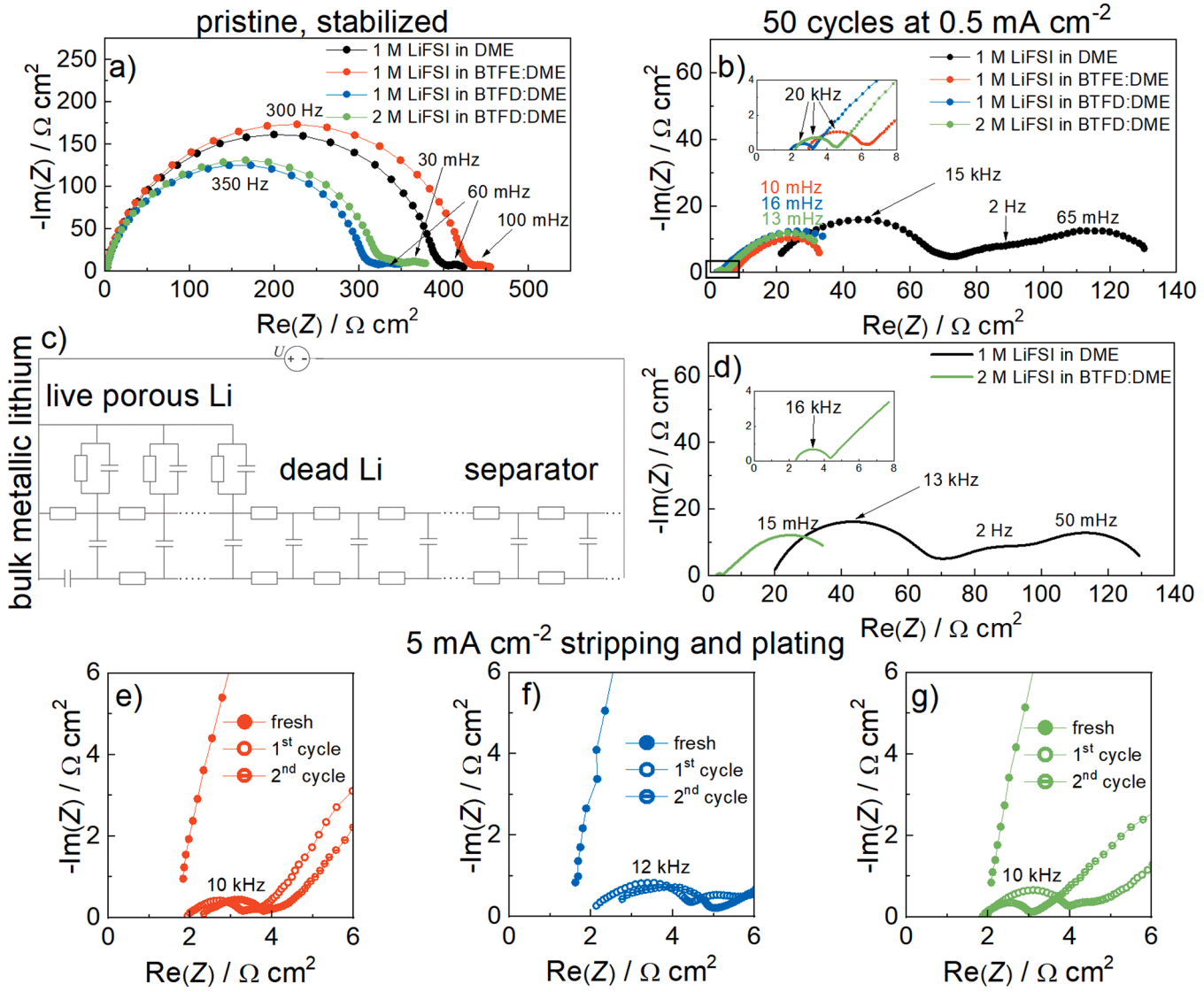

Fig. 2. Impedance spectroscopy analysis of the Li metal anode performance in the electrolytes. Impedance spectra of: (a) non-cycled stabilized Li||Li symmetrical cells and (b) the same cells after 50 cycles of stripping and plating at a current density of 0.5 mA cm^{-2} to the limit of 1.0 mAh cm^{-2}. (c) The TLM circuit used to simulate the spectra of the cycled Li||Li cells. For circuit element indexation, the reader is referred to Fig. S14. (d) Impedance spectra simulation of the 1 M LiFSI in DME and 2 M LiFSI in BTFD:DME cell spectra from (b) using the TLM model from (c). (e, f, g) High-frequency region of impedance spectra for symmetrical Li||Li cells with 1 M LiFSI in BTFE:DME, 1 M LiFSI in BTFD:DME and 2 M LiFSI in BTFD:DME, respectively, which all underwent stripping and plating at 5 mA cm^{-2} to the limit of 10 mAh cm^{-2}.

from short-circuit formation and extensive passivation of the deposited lithium, which is in line with the Li||Cu cell data reported in Fig. 1d. The SEM micrographs of the cycled electrode (Fig. S17a-c) support the above conclusions as they show a difference in morphology of the high surface area lithium deposits: The total thickness is larger, but the coverage is less uniform. In comparison with the BTFD based electrolyte, a single Li deposit is also thinner (Fig. S18), indicating a higher surface area and consequently higher tendency of electrolyte consumption and increased formation of "dead" Li. The direction of growth for some of the deposits (*e.g.* those marked with an arrow in Fig. S17b) appear to be perpendicular to the electrode (thicknesses reaching over 30 μm) and could signal a higher tendency for short-circuit formation.

To further highlight differences between the fluorinated ether-based electrolytes, stripping and plating under aggravated cycling conditions were conducted. There is again little difference between the EIS spectra, with the exception of the stability of the resistive intercept (Figs 2e-f, Fig. S19). For the cells with the 1 M LiFSI in BTFE:DME (Fig. 2e) and 1 M LiFSI in BTFD:DME (Fig. 2f) electrolytes, the resistive intercept increases by roughly 30% from 1.8 to 2.4 Ωcm^2, which suggests significant electrolyte decomposition taking place. In contrast, the 2 M LiFSI in BTFD:DME electrolyte based cell keeps the resistive intercept roughly constant, hence indicating limited electrolyte decomposition – if any.

After evaluating the performance of the electrolytes using lithium metal anodes in Li||Cu and Li||Li cells, we turn to full cell performance using LTO and NMC811 cathodes (Fig. 3). Here, the Li||LTO cells with the BTFE and BTFD-based electrolytes both display increased cycling stability as compared to the cells using the 1 M LiFSI in DME reference electrolyte (Fig. 3a and Fig. S20). For the Li||NMC811 cells (Fig. 3b and Fig. S21), the use of the 1 M LiFSI in DME reference electrolyte led to rapid cell failure, which we attribute to poor high-voltage stability, while the cells using the fluorinated diluent based electrolytes show both higher capacities as well as improved cycling stabilities, with the best capacity retention obtained for the cell using the 2 M LiFSI in BTFD:DME electrolyte. The reproducibility of data when employing the BTFD-based electrolytes is shown in Fig. S22. Moreover, BTFD-based electrolytes were examined under additional different cycling conditions. In

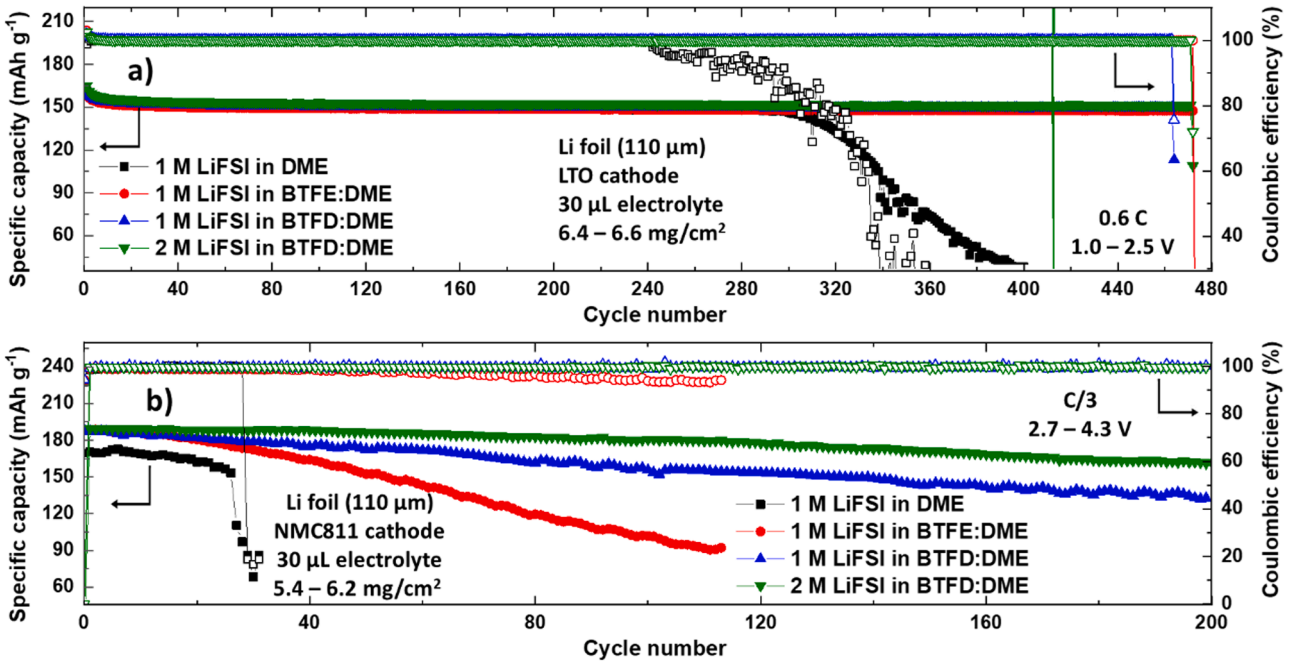

Fig. 3. Electrochemical cycling performance comparison of Li||LTO and Li||NMC811 full cells: (a) Li||LTO full cells at 0.6 C and (b) Li||NMC811 full cells at 0.3 C after two formation cycles at 0.1 C.

Fig. S23, the stable cycling performance of BTFD-based electrolytes with a higher mass loading of NMC811 (16 mg cm^{-2}) coupled with thinner Li foil (50 µm) is demonstrated. Additionally, the BTFD-based electrolytes were evaluated in a Li||NMC811 cell with a high cut-off voltage of 4.6 V (Fig. S24) and exhibited consistent capacity retention, even outperforming TTE-based electrolytes (Fig. S25), supporting the potential of BTFD diluent use in high-voltage LMBs.

From the above, the cyclic and linear fluorinated ether-based electrolytes perform rather similarly in the Li||LTO cells, but the former improves the Li||NMC811 cell performance – which we attribute to several factors; First, LTO is a zero-strain material that operates at a low-medium electrochemical potential [53], thus not challenging the electrolyte oxidative stability, which is why aggravated conditions (Figs. 1 and 2) are needed to see any noticeable differences between the fluorinated electrolytes. Second, NMC811, on the other hand, operates at significantly higher electrochemical potential, which means that the electrolyte oxidative stability (Fig. 1 g) is challenged, showing one advantage of cyclic fluorinated ethers. Furthermore, the cell performance is also highly dependent on the cathode-electrolyte compatibility and the nature and stability of the CEI created [54]. To further understand the clearly noticeable differences between the Li||NMC811 cells using the BTFE- and BTFD-based electrolytes, we conducted several surface analyses of the cycled NMC811 cathodes.

The XPS F 1*s* spectra reveal the presence of two different chemical states of F in the CEI (Figs. 4a–d), which we assign to Li–F (685 eV) and C–F/S–F bonds (688.4 eV) [55]. Both the Li–F and S–F bonds are likely mainly originating from decomposition of the FSI anion [56], while the C-F bond may originate from interaction with the fluorinated diluents [57]. The O 1*s* XPS spectra show at least three peaks, originating from S-O/N—O bonds (532.8 eV), C = O bonds (531.6 eV), and M-O bonds (529.7 eV), where the latter stem from lattice oxygen [58](Fig. 4e–f). Moving from the reference electrolyte, first to the BTFE and then to the BTFD-based electrolytes show increasing ratios between the Li-F and C-F/S-F peaks in the XPS spectra (Figs. 4a–d). Furthermore, in the O 1*s* spectra the M-O relative and absolute intensity both decrease (Fig. 4e–f). This indicates that the CEI resulting from using DME- and BTFE-based electrolytes contains modified bulk NMC transition metals that are still bound to O atoms, in either crystalline or amorphous state. In the case of BTFD-based electrolytes, the M-O contribution significantly decreases with increasing LiFSI concentration in the electrolyte. By correlating this with the increased amount of LiF observed in the F 1*s* spectra, we conclude that CEIs in the latter two electrolytes contain mainly products of decomposed solvents, while the bulk NMC structure underneath remains more or less intact. Additionally, the Li 1*s* spectra are consistent with the F 1*s* spectra, confirming the presence of LiF in the CEI (Fig. S26), while the C 1*s* spectra show the presence of organic species from decomposed solvents (Fig. S27) [59].

We have conducted additional XPS measurements on the cycled Li anode extracted from Li||NMC811 cells after 50 cycles to characterize the Li SEI. The C 1*s*, F 1*s*, S 2*p* and N 1*s* XPS spectra are shown in Fig. S28. As depicted in Fig. S28a, Li electrodes cycled using the BTFD-based electrolytes exhibit lower relative intensities of the CO_3^{2-} and C = O peaks as compared to those cycled in the BTFE-based and the 1 M LiFSI in DME reference electrolytes. This suggests that different solvent decomposition products are formed using the BTFD-based electrolytes. The F 1*s*, S 2*p*, and N 1*s* XPS spectra represent the presence of inorganic components formed in the SEI, primarily originating from the decomposition of the LiFSI salt. As illustrated in Fig. S28b, an increased LiF peak was observed in the case of the BTFD-based electrolytes. Additionally, larger SO_x, S_n^{2-}, and S^{2-} signals were clearly detected (Fig. S28c) and apparent signals of Li_3N were observed in the N 1*s* spectra (Fig. S28d) of Li metal. This collectively suggests that rather than the solvent, LiFSI is preferentially decomposed in the BTFD-based electrolytes to form an anion-derived SEI on the Li metal anode.

The ABF-STEM and HAADF-STEM images (Fig.4e-l) show both the CEIs and the layered structure of the NMC811, with significantly differences for the former. For instance, the ABF-STEM of NMC811 cycled using the 1 M LiFSI in DME electrolyte shows degradation and has the thickest CEI: 4.8 nm (Fig. 4i). In contrast, the NMC811 cycled using the 1 M LiFSI in BTFE:DME electrolyte show a thinner CEI (3.3 nm, Fig. 4j), and even thinner CEIs (2.1–2.4 nm, Fig. 4k and l) were formed using the BTFD-based electrolytes. All CEIs seem to contain both crystalline and amorphous regions, with those from the 1 M LiFSI in DME and 1 M LiFSI in BTFE:DME cells showing an atomic arrangement that differs significantly from bulk NMC811 (Fig. 4i, m, j, n), and resembles <111> rock salt and ⟨110⟩ inverse spinel structures. For the cathodes from the LiFSI

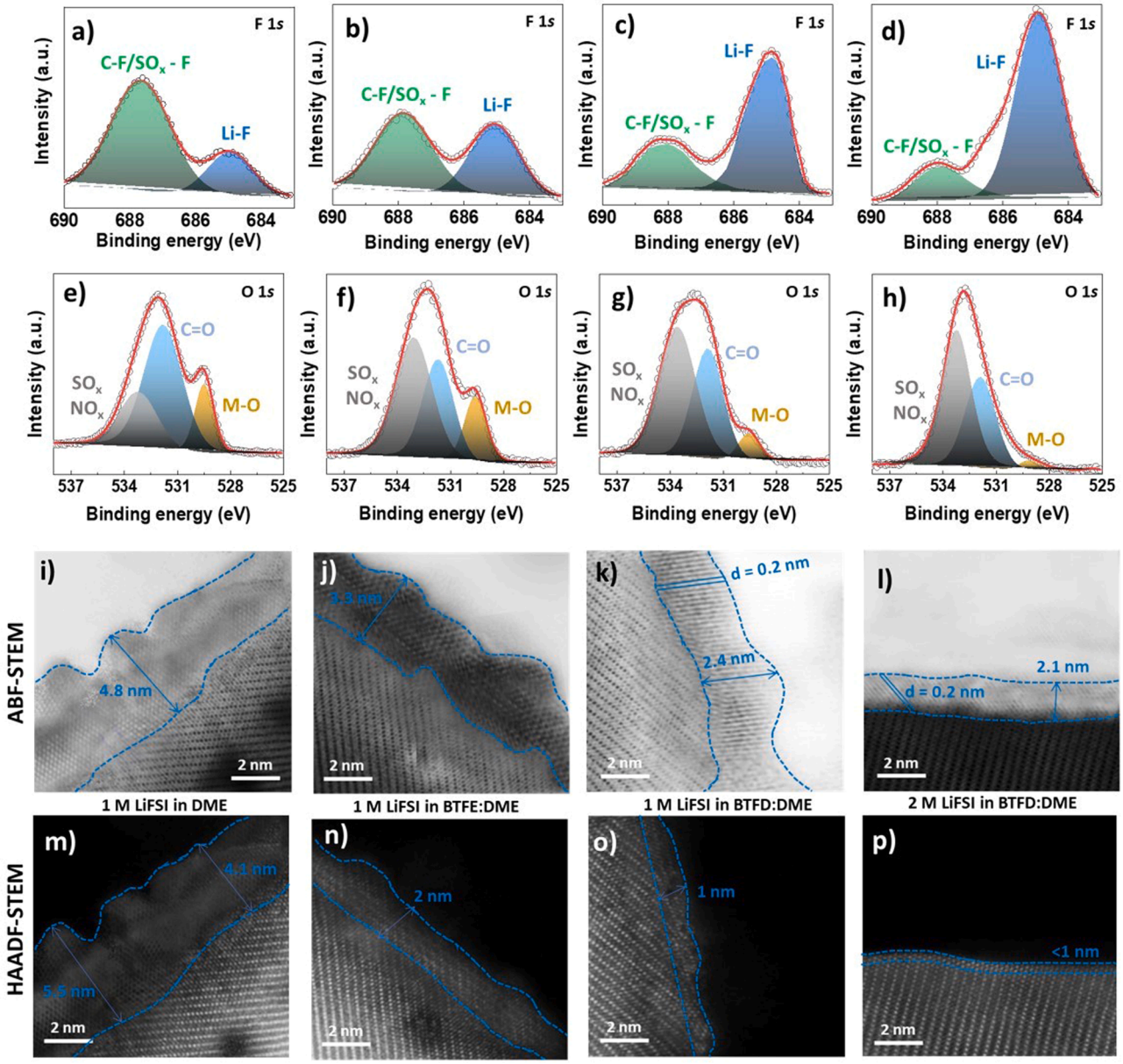

Fig. 4. Surface analyses of (the CEI at) the cycled NMC811 cathodes. F 1*s* XPS (a–d), O 1*s* XPS (e–h), ABF – STEM (i–l) and HAADF – STEM (m–p) imaging of cathodes extracted from cells cycled using different electrolytes: 1 M LiFSI in DME (a, e, i, m), 1 M LiFSI in BTFE:DME (b, f, j, n), 1 M LiFSI in BTFD:DME (c, g, k, o), and 2 M LiFSI in BTFD:DME (d, h, l, p).

in BTFD:DME electrolyte cycled cells, the termination of the NMC811 bulk has an arrangement of the atomic planes with *d* spacings of *ca.* 0.2 nm, which can be assumed to be LiF [59,60], in agreement with the XPS F 1 s analysis (Fig. 4c, d). Some disturbed NMC811 crystal planes can be seen for the 1 M electrolyte (Fig. 4o), while the 2 M electrolyte (Fig. 4p) seems to have a less than 1 nm thin layer with a crystal structure differing from that of bulk NMC811 [56,61,62]. For the latter it is unclear whether the surface termination of the NMC811 existed before cycling or if it was formed during the cycling.

The final surface analysis was made by STEM imaging, which overall indicates that the NMC811 cathodes cycled using the BTFD-based electrolytes are less degraded. This is signified by the thinner layer of altered crystal structure on the surfaces of the NMC811 particles (Fig. 4m-p). Altogether, moving from the 1 M LiFSI in DME reference electrolyte to the BTFE-based electrolyte and finally to BTFD-based electrolytes, the CEI changes its thickness and composition. The main observation for the BTFD-based electrolytes is the LiF-based crystalline CEI layer improving its stability [63,64] and decreasing NMC811 degradation and disordered rock salt formation – which explains the improved electrochemical performance (Fig. 3b).

The above observed and highly beneficial SEI and CEI must in some way originate from the electrolyte. In this regard, Lu *et* al. [29,30] studied the solvation structures of the LHCEs and found that the fluoroethers have relatively weaker coordination with Li^+ and stronger coordination with FSI. Additionally, according to the literature [65–67] SEI/CEI properties correlate to the cation solvation, as solvents in the cation first solvation shell are more likely to interact with the electrode surface and decompose to form the CEI, and we here therefore address cation solvation changes by both Raman and NMR spectroscopies. The Raman spectrum of the 1 M LiFSI in DME electrolyte (Fig. 5a) shows two additional peaks at 717 and 885 cm^{-1} as compared to the spectrum of pure DME, which we assign to "free" FSI anion [68] and to Li^+ solvated by DME (Li^+ - DME), respectively. As BTFE is introduced, the former peak decreases in intensity and is slightly shifted, to 733 cm^{-1}, which

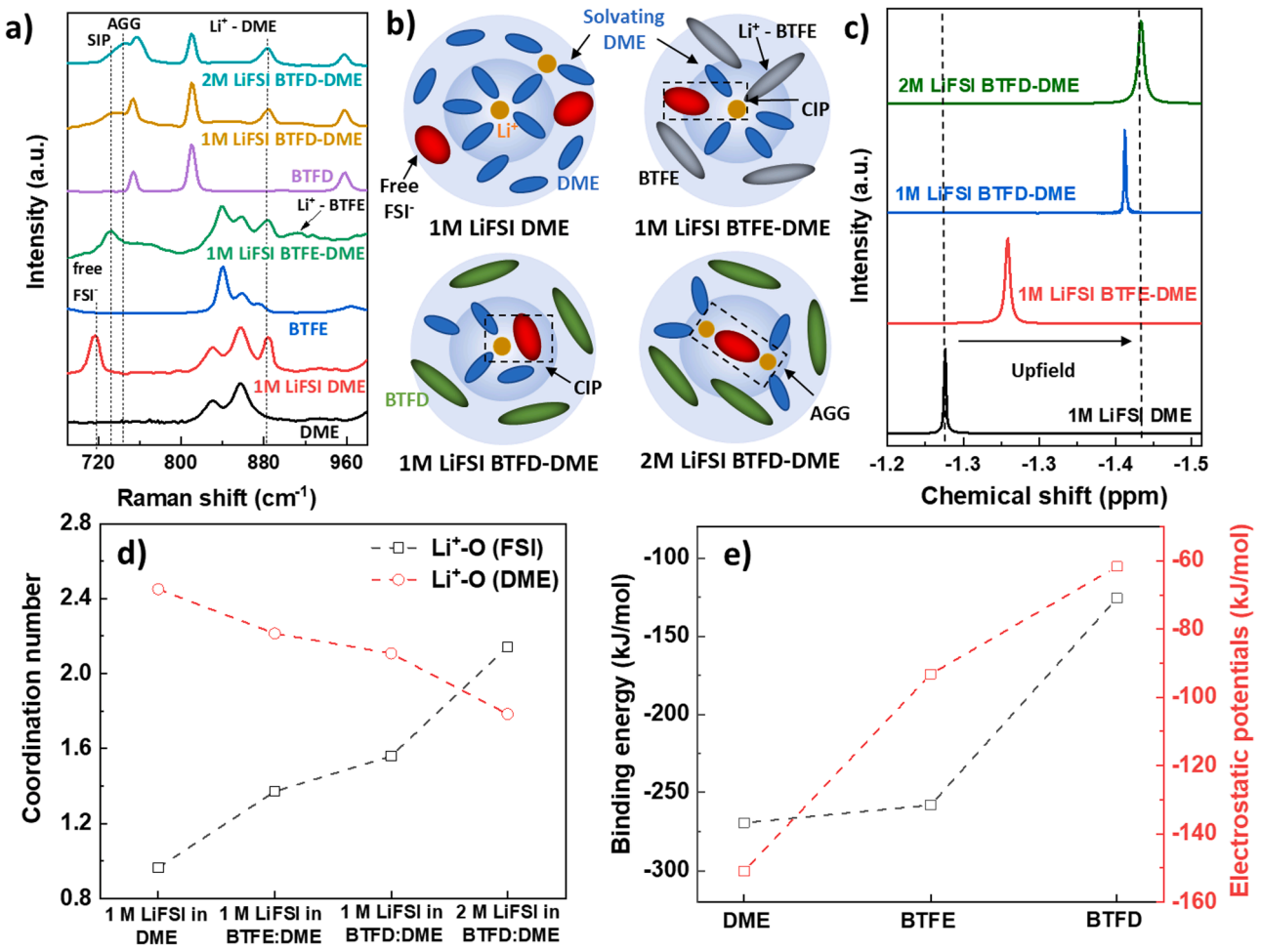

Fig. 5. The solvation structures within the electrolytes: (a) Raman spectra of solvents, diluents, and electrolytes, (b) Schematic illustration of the Li^+ solvation structures in the different electrolytes, (c) ^7Li NMR spectra, (d) Li^+-O CNs from the MD simulations, and (e) Binding energies of Li^+ and ESPs of DME, BTFE, and BTFD from the DFT calculations.

indicates the formation of contact ion-pairs (CIPs, Li^+-FSI). The additional peaks that emerge at *ca.* 915 cm^{-1} could be ascribed to Li^+-BTFE interactions.

In the 1 M LiFSI in BTFD:DME electrolyte spectrum the peak corresponding to ''free'' FSI anion both broadens and shifts slightly, to 747 cm^{-1}, which suggests creation of aggregates/triplets (AGGs) [69], alongside the CIPs, which also increase as a function of salt concentration. Looking at the spectral region containing the BTFD peaks, *e.g.* at *ca.* 810 cm^{-1}, we do not observe any shifts from the pure BTFD spectrum in neither the 1 nor the 2 M BTFD electrolyte spectra. Thus, BTFD does not seem to take part in the cation solvation and is hence a diluent and not a co-solvent. The schematic Fig. 5b illustrates the solvation structures based on the Raman results.

The ^7Li NMR spectra similarly showed an upfield shift for the BTFD-based electrolytes (Fig. 5c), which we attribute to stronger cation-anion interactions as this increases the electron density around Li^+ [70]. A similar trend was also observed in the ^{19}F NMR spectra (Fig. S29).

To further support the Raman and NMR results, the analysis of the RDFs and CNs calculated from the MD simulation data (Fig. 5d) shows that Li^+ is primarily coordinated by DME and FSI (see also Fig. S30). For all but the 2 M LiFSI in BTFD:DME electrolyte Li^+ predominantly interacts with DME, with DME CNs decreasing from 2.5 to 1.8 and simultaneously the FSI CNs increase from 1.0 to 2.1. Thus, while the diluents, BTFE and BTFD, likely are largely absent from the first cation solvation shell (Fig. S30), they anyhow significantly impact the ion-ion and ion-solvent interactions. However, for BTFE the MD simulation results and the experimental observations with respect to coordination cannot be reconciled in detail, possibly due to that, the employed non-polarizable FFs in the former overstructur the solvent, which reduces the response to weak electrostatic interactions. As the FSI CN is larger than the DME CN for the 2 M LiFSI in BTFD:DME electrolyte, this could truly be classified as a HCE. We note in passing that the total CN is close to constant for all the 1 M electrolytes – *ca.* 3.6 – and only slightly increases for the 2 M electrolyte (*ca.* 3.9).

The classical picture from the MD simulations, that arguably is highly dependent on the FF used, is complemented by DFT calculated ion-solvent/diluent binding energies as well as ESPs of the solvents (Fig. 5e and S31). This confirms the much weaker affinity of BTFD towards Li^+ as compared to BTFE and DME, both having the same -O-CH_2—CH_2—O- moiety in their structure, which explains their relatively strong (and similar) binding towards Li^+ [24]. This is also corroborated by the ESPs showing the more negative potential on the oxygen atoms for DME and BTFE in comparison to BTFD (Fig. 5e and S32).

4. Conclusions

The cyclic fluorinated ether, BTFD, acts as a diluent in BTFD-based electrolytes, which improves the CE with respect to lithium metal stripping and plating by reducing the formation of 'dead Li', while also allowing for the enhanced cycling performance of Li||NMC811 cells. This all stems from modified CEIs (more LiF-rich) which arise from an altered Li^+-solvation in the electrolytes - the electrolyte shows larger

propensity for Li^+-FSI interactions, which brings more FSI closer to the electrode surface. Hence, we can conclude that the cyclic fluorinated ether BTFD provides a way to largely and synergistically solve the challenges of both the lithium metal anode and high-voltage cathode(s). The study attests to the importance of the cyclic molecular structure of fluorinated ethers in improving electrolytes for high-voltage LMBs.

CRediT authorship contribution statement

Hafiz Ahmad Ishfaq: Writing – original draft, Visualization, Investigation, Data curation. **Carolina Cruz Cardona:** Formal analysis, Data curation. **Elena Tchernychova:** Formal analysis, Data curation. **Patrik Johansson:** Writing – review & editing, Supervision. **Robert Dominko:** Writing – review & editing, Funding acquisition. **Sara Drvarič Talian:** Writing – original draft, Supervision, Methodology, Conceptualization.

Declaration of competing interest

The authors declare the following financial interests/personal relationships which may be considered as potential competing interests: co-authors serving as guest editors for Alistore-ERI special issue - Robert Dominko and Patrik Johansson If there are other authors, they declare that they have no known competing financial interests or personal relationships that could have appeared to influence the work reported in this paper.

Acknowledgements

The authors acknowledge the funding from the DESTINY PhD programme (European Union's Horizon2020 research and innovation program under the Marie Skłodowska-Curie Actions COFUND Grant Agreement #945357) and the additional financial support by the Slovenian Research Agency ARRS (core program funding P2–0423) and from VINNOVA/Batteries Sweden (BASE) (grant 2019–00064). CCC, HAI, and PJ are in addition grateful for the computational resources (Tetralith) provided by the Swedish National Infrastructure for Computing (SNIC) at the National Supercomputing Centre (NSC). PJ is also grateful for the financial support from his Swedish Research Council (VR) Distinguished Professor grant 'Next Generation Batteries' (#2021–00613). We would also like to acknowledge Jože Grdadolnik for the Raman spectroscopy measurements and Svit Menart for the help with the NMR spectroscopy measurements, both from NIC, Ljubljana, and Stefan Freunberger for allowing us to use their in-house built setup for ionic conductivity measurements of electrolytes at the Institute of Science and Technology, Austria (ISTA).

Supplementary materials

Supplementary material associated with this article can be found, in the online version, at doi:10.1016/j.ensm.2024.103375.

References

[1] K. Xu, Nonaqueous liquid electrolytes for lithium-based rechargeable batteries, Chem. Rev. 104 (2004), https://doi.org/10.1021/cr030203g.
[2] X.B. Cheng, R. Zhang, C.Z. Zhao, Q. Zhang, Toward safe lithium metal anode in rechargeable batteries: a review, Chem. Rev. (2017) 117, https://doi.org/10.1021/acs.chemrev.7b00115.
[3] E.M. Erickson, E. Markevich, G. Salitra, D. Sharon, D. Hirshberg, E. de la Llave, I. Shterenberg, A. Rosenman, A. Frimer, D. Aurbach, Review—development of advanced rechargeable batteries: a continuous challenge in the choice of suitable electrolyte Solutions, J. Electrochem. Soc. (2015) 162, https://doi.org/10.1149/2.0051514jes.
[4] D. Lin, Y. Liu, Y. Cui, Reviving the lithium metal anode for high-energy batteries, Nat. Nanotechnol. (2017) 12, https://doi.org/10.1038/nnano.2017.16.
[5] P. Albertus, S. Babinec, S. Litzelman, A. Newman, Status and challenges in enabling the lithium metal electrode for high-energy and low-cost rechargeable batteries, Nat. Energy. 3 (2018), https://doi.org/10.1038/s41560-017-0047-2.
[6] M. Winter, B. Barnett, K. Xu, Before Li ion batteries, Chem. Rev. 118 (2018), https://doi.org/10.1021/acs.chemrev.8b00422.
[7] D. Aurbach, Review of selected electrode-solution interactions which determine the performance of Li and Li ion batteries, J. Power Sources. 89 (2000), https://doi.org/10.1016/S0378-7753(00)00431-6.
[8] X. Yu, A. Manthiram, Electrode-electrolyte interfaces in lithium-based batteries, Energy Environ. Sci. 11 (2018), https://doi.org/10.1039/c7ee02555f.
[9] Y.K. Liu, C.Z. Zhao, J. Du, X.Q. Zhang, A.B. Chen, Q. Zhang, Research progresses of liquid electrolytes in Lithium-ion batteries, Small 19 (2023), https://doi.org/10.1002/smll.202205315.
[10] H. Adenusi, G.A. Chass, S. Passerini, K.V. Tian, G. Chen, Lithium batteries and the solid electrolyte interphase (SEI)—progress and outlook, Adv. Energy Mater. 13 (2023), https://doi.org/10.1002/aenm.202203307.
[11] B. Wu, C. Chen, L.H.J. Raijmakers, J. Liu, D.L. Danilov, R.A. Eichel, P.H.L. Notten, Li-growth and SEI engineering for anode-free Li-metal rechargeable batteries: a review of current advances, Energy Storage Mater 57 (2023), https://doi.org/10.1016/j.ensm.2023.02.036.
[12] C. Fang, J. Li, M. Zhang, Y. Zhang, F. Yang, J.Z. Lee, M.H. Lee, J. Alvarado, M. A. Schroeder, Y. Yang, B. Lu, N. Williams, M. Ceja, L. Yang, M. Cai, J. Gu, K. Xu, X. Wang, Y.S. Meng, Quantifying inactive lithium in lithium metal batteries, Nature (2019) 572, https://doi.org/10.1038/s41586-019-1481-z.
[13] W. Li, H. Yao, K. Yan, G. Zheng, Z. Liang, Y.M. Chiang, Y. Cui, The synergetic effect of lithium polysulfide and lithium nitrate to prevent lithium dendrite growth, Nat. Commun. 6 (2015), https://doi.org/10.1038/ncomms8436.
[14] J. Zhang, H. Zhang, L. Deng, Y. Yang, L. Tan, X. Niu, Y. Chen, L. Zeng, X. Fan, Y. Zhu, An additive-enabled ether-based electrolyte to realize stable cycling of high-voltage anode-free lithium metal batteries, Energy Storage Mater 54 (2023), https://doi.org/10.1016/j.ensm.2022.10.052.
[15] J. Zhang, Q. Li, Y. Zeng, Z. Tang, D. Sun, D. Huang, Y. Tang, H. Wang, Weakly solvating cyclic ether electrolyte for high-voltage lithium metal batteries, ACS Energy Lett 8 (2023), https://doi.org/10.1021/acsenergylett.3c00181.
[16] J. Qian, W.A. Henderson, W. Xu, P. Bhattacharya, M. Engelhard, O. Borodin, J. G. Zhang, High rate and stable cycling of lithium metal anode, Nat. Commun. 6 (2015), https://doi.org/10.1038/ncomms7362.
[17] S. Jiao, X. Ren, R. Cao, M.H. Engelhard, Y. Liu, D. Hu, D. Mei, J. Zheng, W. Zhao, Q. Li, N. Liu, B.D. Adams, C. Ma, J. Liu, J.G. Zhang, W. Xu, Stable cycling of high-voltage lithium metal batteries in ether electrolytes, Nat. Energy. 3 (2018), https://doi.org/10.1038/s41560-018-0199-8.
[18] Q. Zhao, S. Stalin, L.A. Archer, Stabilizing metal battery anodes through the design of solid electrolyte interphases, Joule 5 (2021), https://doi.org/10.1016/j.joule.2021.03.024.
[19] Y. Xiao, X. Wang, K. Yang, J. Wu, Y. Chao, C. Xi, M. Li, Q. Zhang, Z. Liu, L. Li, Y. Yu, C. Yang, The anion-dominated dynamic coordination field in the electrolytes for high-performance lithium metal batteries, Energy Storage Mater 55 (2023), https://doi.org/10.1016/j.ensm.2022.12.038.
[20] S. Chen, J. Zheng, D. Mei, K.S. Han, M.H. Engelhard, W. Zhao, W. Xu, J. Liu, J. G. Zhang, High-voltage lithium-metal batteries enabled by localized high-concentration electrolytes, Adv. Mater. 30 (2018), https://doi.org/10.1002/adma.201706102.
[21] X. Cao, H. Jia, W. Xu, J.-G. Zhang, Review—localized high-concentration electrolytes for lithium batteries, J. Electrochem. Soc. 168 (2021), https://doi.org/10.1149/1945-7111/abd60e.
[22] S. Drvarič Talian, S. Jeschke, A. Vizintin, K. Pirnat, I. Arčon, G. Aquilanti, P. Johansson, R. Dominko, Fluorinated ether based electrolyte for high-energy lithium-sulfur batteries: Li+ solvation role behind reduced polysulfide solubility, Chem. Mater. 29 (2017), https://doi.org/10.1021/acs.chemmater.7b03654.
[23] S. Zhu, J. Chen, Dual strategy with Li-ion solvation and solid electrolyte interphase for high Coulombic efficiency of lithium metal anode, Energy Storage Mater 44 (2022), https://doi.org/10.1016/j.ensm.2021.10.007.
[24] Y. Zhao, T. Zhou, L.P.H. Jeurgens, X. Kong, J.W. Choi, A. Coskun, Electrolyte engineering for highly inorganic solid electrolyte interphase in high-performance lithium metal batteries, Chem 9 (2023), https://doi.org/10.1016/j.chempr.2022.12.005.
[25] Y. Zhao, T. Zhou, M. El Kazzi, A. Coskun, Fluorinated cyclic ether co-solvents for ultra-high-voltage practical lithium-metal batteries, ACS Appl. Energy Mater. 5 (2022), https://doi.org/10.1021/acsaem.2c01261.
[26] Y. Zhao, T. Zhou, D. Baster, M. El Kazzi, J.W. Choi, A. Coskun, Targeted functionalization of cyclic ether solvents for controlled reactivity in high-voltage lithium metal batteries, ACS Energy Lett 8 (2023), https://doi.org/10.1021/acsenergylett.3c01004.
[27] Y. Zhao, T. Zhou, T. Ashirov, M. El Kazzi, C. Cancellieri, L.P.H. Jeurgens, J.W. Choi, A. Coskun, Fluorinated ether electrolyte with controlled solvation structure for high voltage lithium metal batteries, Nat. Commun. 13 (2022), https://doi.org/10.1038/s41467-022-29199-3.
[28] M. Wu, Z. Wang, W. Zhang, C. Jayawardana, Y. Li, F. Chen, B. Nan, B.L. Lucht, C. Wang, High-performance lithium metal batteries enabled by a fluorinated cyclic ether with a low reduction potential, Angew. Chemie - Int. Ed 62 (2023), https://doi.org/10.1002/anie.202216169.
[29] G. Zhang, J. Li, S. Sen Chi, J. Wang, Q. Wang, R. Ke, Z. Liu, H. Wang, C. Wang, J. Chang, Y. Deng, J. Lu, Molecular design of competitive solvation electrolytes for practical high-energy and long-cycling lithium-metal batteries, Adv. Funct. Mater. 2312413 (2023) 1–11, https://doi.org/10.1002/adfm.202312413.
[30] G. Zhang, J. Chang, L. Wang, J. Li, C. Wang, R. Wang, G. Shi, K. Yu, W. Huang, H. Zheng, T. Wu, Y. Deng, J. Lu, A monofluoride ether-based electrolyte solution for fast-charging and low-temperature non-aqueous lithium metal batteries, Nat. Commun. 14 (2023), https://doi.org/10.1038/s41467-023-36793-6.

[31] B.D. Adams, J. Zheng, X. Ren, W. Xu, J.G. Zhang, Accurate determination of coulombic efficiency for lithium metal anodes and lithium metal batteries, Adv. Energy Mater. 8 (2018), https://doi.org/10.1002/aenm.201702097.
[32] Y. Lu, C.Z. Zhao, H. Yuan, X.B. Cheng, J.Q. Huang, Q. Zhang, Critical current density in solid-state lithium metal batteries: mechanism, influences, and strategies, Adv. Funct. Mater. 31 (2021) 1–33, https://doi.org/10.1002/adfm.202009925.
[33] P.G. Bruce, M.T. Hardgrave, C.A. Vincent, Steady state current flow in solid binary electrolyte cells. Part 2. The effect of ion association, J. Electroanal. Chem. (1989) 271, https://doi.org/10.1016/0022-0728(89)80061-0.
[34] P.G. Bruce, C.A. Vincent, Steady state current flow in solid binary electrolyte cells, J. Electroanal. Chem. (1987) 225, https://doi.org/10.1016/0022-0728(87)80001-3.
[35] S. Drvarič Talian, J. Bobnar, A.R. Sinigoj, I. Humar, M. Gaberšček, Transmission line model for description of the impedance response of Li electrodes with dendritic growth, J. Phys. Chem. C. (2019) 123, https://doi.org/10.1021/acs.jpcc.9b05887.
[36] S. Drvarič Talian, J. Moškon, R. Dominko, M. Gaberšček, Impedance response of porous carbon cathodes in polysulfide redox system, Electrochim. Acta. (2019) 302, https://doi.org/10.1016/j.electacta.2019.02.037.
[37] S. Drvarič Talian, G. Kapun, J. Moškon, R. Dominko, M. Gaberšček, Transmission line model impedance analysis of lithium sulfur batteries: influence of lithium sulfide deposit formed during discharge and self-discharge, J. Electrochem. Soc. (2022) 169, https://doi.org/10.1149/1945-7111/ac4a4e.
[38] Y. Zhao, D.G. Truhlar, The M06 suite of density functionals for main group thermochemistry, thermochemical kinetics, noncovalent interactions, excited states, and transition elements: two new functionals and systematic testing of four M06-class functionals and 12 other functionals, Theor. Chem. Acc. (2008) 120, https://doi.org/10.1007/s00214-007-0310-x.
[39] Y. Zhao, D.G. Truhlar, Density functionals with broad applicability in chemistry, Acc. Chem. Res. 41 (2008), https://doi.org/10.1021/ar700111a.
[40] C.G. Zhan, J.A. Nichols, D.A. Dixon, Ionization potential, electron affinity, electronegativity, hardness, and electron excitation energy: molecular properties from density functional theory orbital energies, J. Phys. Chem. A. (2003) 107, https://doi.org/10.1021/jp0225774.
[41] Z. Zhang, L. Hu, H. Wu, W. Weng, M. Koh, P.C. Redfern, L.A. Curtiss, K. Amine, Fluorinated electrolytes for 5 v lithium-ion battery chemistry, Energy Environ. Sci. 6 (2013), https://doi.org/10.1039/c3ee24414h.
[42] M.J. Frisch, G.W. Trucks, H.B. Schlegel, G.E. Scuseria, M.A. Robb, J.R. Cheeseman, G. Scalmani, V. Barone, B. Mennucci, G.A. Petersson, Gaussian 09, Revision A. 02, Gaussian, Inc., Wallingford CT, 2016.
[43] S. Plimpton, Fast parallel algorithms for short-range molecular dynamics, J. Comput. Phys. (1995) 117, https://doi.org/10.1006/jcph.1995.1039.
[44] W.L. Jorgensen, D.S. Maxwell, J. Tirado-Rives, Development and testing of the OPLS all-atom force field on conformational energetics and properties of organic liquids, J. Am. Chem. Soc. 118 (1996), https://doi.org/10.1021/ja9621760.
[45] W.L. Jorgensen, J. Tirado-Rives, Potential energy functions for atomic-level simulations of water and organic and biomolecular systems, Proc. Natl. Acad. Sci. U.S.A. (2005) 102, https://doi.org/10.1073/pnas.0408037102.
[46] L.S. Dodda, I.C. De Vaca, J. Tirado-Rives, W.L. Jorgensen, LigParGen web server: an automatic OPLS-AA parameter generator for organic ligands, Nucleic Acids Res (2017) 45, https://doi.org/10.1093/nar/gkx312.
[47] L.S. Dodda, J.Z. Vilseck, J. Tirado-Rives, W.L. Jorgensen, 14*CM1A-LBCC: localized bond-charge corrected CM1A charges for condensed-phase simulations, J. Phys. Chem. B. 1 (2017) 121, https://doi.org/10.1021/acs.jpcb.7b00272.
[48] A.A.H. Pádua, Resolving dispersion and induction components for polarisable molecular simulations of ionic liquids, J. Chem. Phys. (2017) 146, https://doi.org/10.1063/1.4983687.
[49] J. Self, K.D. Fong, K.A. Persson, Transport in Superconcentrated LiPF6 and LiBF4/Propylene carbonate electrolytes, ACS Energy Lett 4 (2019), https://doi.org/10.1021/acsenergylett.9b02118.
[50] Z. Yu, P.E. Rudnicki, Z. Zhang, Z. Huang, H. Celik, S.T. Oyakhire, Y. Chen, X. Kong, S.C. Kim, X. Xiao, H. Wang, Y. Zheng, G.A. Kamat, M.S. Kim, S.F. Bent, J. Qin, Y. Cui, Z. Bao, Rational solvent molecule tuning for high-performance lithium metal battery electrolytes, Nat. Energy. 7 (2022), https://doi.org/10.1038/s41560-021-00962-y.
[51] S. Drvarič Talian, J. Bobnar, J. Moškon, R. Dominko, M. Gaberšček, Effect of high concentration of polysulfides on Li stripping and deposition, Electrochim. Acta. (2020) 354, https://doi.org/10.1016/j.electacta.2020.136696.
[52] Q. Li, A. Chen, D. Wang, Z. Pei, C. Zhi, Soft shorts" Hidden in Zinc metal anode research, Joule 6 (2022), https://doi.org/10.1016/j.joule.2021.12.009.
[53] T.F. Yi, S.Y. Yang, Y. Xie, Recent advances of Li4Ti5O12 as a promising next generation anode material for high power lithium-ion batteries, J. Mater. Chem. A. (2015) 3, https://doi.org/10.1039/c4ta06882c.
[54] Y. Wu, X. Liu, L. Wang, X. Feng, D. Ren, Y. Li, X. Rui, Y. Wang, X. Han, G.L. Xu, H. Wang, L. Lu, X. He, K. Amine, M. Ouyang, Development of cathode-electrolyte-interphase for safer lithium batteries, Energy Storage Mater 37 (2021), https://doi.org/10.1016/j.ensm.2021.02.001.
[55] C. Xu, F. Lindgren, B. Philippe, M. Gorgoi, F. Björefors, K. Edström, T. Gustafsson, Improved performance of the silicon anode for li-ion batteries: understanding the surface modification mechanism of fluoroethylene carbonate as an effective electrolyte additive, Chem. Mater. (2015) 27, https://doi.org/10.1021/acs.chemmater.5b00339.
[56] X. Cao, P. Gao, X. Ren, L. Zou, M.H. Engelhard, B.E. Matthews, J. Hu, C. Niu, D. Liu, B.W. Arey, C. Wang, J. Xiao, J. Liu, W. Xu, J.G. Zhang, Effects of fluorinated solvents on electrolyte solvation structures and electrode/electrolyte interphases for lithium metal batteries, Proc. Natl. Acad. Sci. U.S.A. (2021) 118, https://doi.org/10.1073/pnas.2020357118.
[57] L. Dong, Y. Liu, K. Wen, D. Chen, D. Rao, J. Liu, B. Yuan, Y. Dong, Z. Wu, Y. Liang, M. Yang, J. Ma, C. Yang, C. Xia, B. Xia, J. Han, G. Wang, Z. Guo, W. He, High-polarity fluoroalkyl ether electrolyte enables solvation-free Li+ transfer for high-rate lithium metal batteries, Adv. Sci. 9 (2022), https://doi.org/10.1002/advs.202104699.
[58] Y. Yu, Y. Zhang, L. Giordano, Y.G. Zhu, F. Maglia, R. Jung, F.S. Gittleson, Y. Shao-Horn, Enhanced Cycling of Ni-Rich Positive Electrodes by Fluorine Modification, J. Electrochem. Soc. (2021) 168, https://doi.org/10.1149/1945-7111/ac0b27.
[59] X. Cao, X. Ren, L. Zou, M.H. Engelhard, W. Huang, H. Wang, B.E. Matthews, H. Lee, C. Niu, B.W. Arey, Y. Cui, C. Wang, J. Xiao, J. Liu, W. Xu, J.G. Zhang, Monolithic solid–electrolyte interphases formed in fluorinated orthoformate-based electrolytes minimize Li depletion and pulverization, Nat. Energy. (2019) 4, https://doi.org/10.1038/s41560-019-0464-5.
[60] C. Wang, Y.S. Meng, K. Xu, Perspective—Fluorinating Interphases, J. Electrochem. Soc. (2019) 166, https://doi.org/10.1149/2.0281903jes.
[61] C. Xu, K. Märker, J. Lee, A. Mahadevegowda, P.J. Reeves, S.J. Day, M.F. Groh, S. P. Emge, C. Ducati, B.Layla Mehdi, C.C. Tang, C.P. Grey, Bulk fatigue induced by surface reconstruction in layered Ni-rich cathodes for Li-ion batteries, Nat. Mater. (2021) 20, https://doi.org/10.1038/s41563-020-0767-8.
[62] L. Zou, P. Gao, H. Jia, X. Cao, H. Wu, H. Wang, W. Zhao, B.E. Matthews, Z. Xu, X. Li, J.G. Zhang, W. Xu, C. Wang, Nonsacrificial additive for tuning the cathode–electrolyte interphase of lithium-ion batteries, ACS Appl. Mater. Interfaces. (2022) 14, https://doi.org/10.1021/acsami.1c20789.
[63] J. Zhi, P. Chen, Design principles for the fabrication of high-performance cathode-electrolyte interphase for Li-ion batteries, One Earth 5 (2022), https://doi.org/10.1016/j.oneear.2022.02.011.
[64] Q. Zhang, J. Ma, L. Mei, J. Liu, Z. Li, J. Li, Z. Zeng, In situ TEM visualization of LiF nanosheet formation on the cathode-electrolyte interphase (CEI) in liquid-electrolyte lithium-ion batteries, Matter 5 (2022), https://doi.org/10.1016/j.matt.2022.01.015.
[65] X. Ren, P. Gao, L. Zou, S. Jiao, X. Cao, X. Zhang, H. Jia, M.H. Engelhard, B. E. Matthews, H. Wu, H. Lee, C. Niu, C. Wang, B.W. Arey, J. Xiao, J. Liu, J.G. Zhang, W. Xu, Role of inner solvation sheath within salt–solvent complexes in tailoring electrode/electrolyte interphases for lithium metal batteries, Proc. Natl. Acad. Sci. U.S.A. (2020) 117, https://doi.org/10.1073/pnas.2010852117.
[66] S. Wang, J. Zhang, W. Hua, L. Wen, G. Tang, X. Wang, C. Ma, W. Chen, Solvation-enhanced electrolyte on layered oxide cathode tailoring even and stable CEI for durable sodium storage, Carbon Neutrality 2 (2023), https://doi.org/10.1007/s43979-023-00060-w.
[67] Z. Piao, P. Xiao, R. Luo, J. Ma, R. Gao, C. Li, J. Tan, K. Yu, G. Zhou, H.M. Cheng, Constructing a Stable Interface Layer by Tailoring Solvation Chemistry in Carbonate Electrolytes for High-Performance Lithium-Metal Batteries, Adv. Mater. (2022) 34, https://doi.org/10.1002/adma.202108400.
[68] J. Scheers, P. Johansson, Publisher's Note, Comment on "Transport and electrochemical properties and spectral features of non-aqueous electrolytes containing LiFSI in linear carbonate solvents [J. Electrochem. Soc., 159, S1 (2012)], J. Electrochem. Soc. 159 (2012), https://doi.org/10.1149/2.jes120006.
[69] P. Jankowski, W. Wieczorek, P. Johansson, New boron based salts for lithium-ion batteries using conjugated ligands, Phys. Chem. Chem. Phys. 18 (2016), https://doi.org/10.1039/c6cp02409b.
[70] Y. Chen, Z. Yu, P. Rudnicki, H. Gong, Z. Huang, S.C. Kim, J.C. Lai, X. Kong, J. Qin, Y. Cui, Z. Bao, Steric effect tuned ion solvation enabling stable cycling of high-voltage lithium metal battery, J. Am. Chem. Soc. (2021) 143, https://doi.org/10.1021/jacs.1c09006.